CHEMISTRY OF MATERIALS
Article
Cite This: Chem. Mater. 2017, 29, 9192-9199
pubs.acs.org/cm

Revealing Cation-Exchange-Induced Phase Transformations in Multielemental Chalcogenide Nanoparticles

Joel M. R. Tan,[†,‡,∥] Mary C. Scott,[⊥,○] Wei Hao,[∥] Tom Baikie,[‡,∥] Christopher T. Nelson,[⊥,○] Srikanth Pedireddy,[§] Runzhe Tao,[⊥,#] Xingyi Ling,[§] Shlomo Magdassi,[◆] Timothy White,[‡,∥] Shuzhou Li,[∥] Andrew M. Minor,[⊥,#,○] Haimei Zheng,[⊥,#] and Lydia H. Wong*[,‡,∥]

[†]Interdisciplinary Graduate School, [‡]Energy Research Institute, [§]Division of Chemistry and Biological Chemistry, School of Physical and Mathematical Sciences, and [∥]School of Materials Science and Engineering, Nanyang Technological University, Singapore 639798

[⊥]Department of Materials Science and Engineering, University of California, Berkeley, California 94720, United States

[#]Materials Sciences Division and [○]National Center for Electron Microscopy, Molecular Foundry, Lawrence Berkeley National Laboratory, Berkeley, California 94720, United States

[◆]The Center for Nanoscience and Nanotechnology, The Hebrew University of Jerusalem, Edmond J. Safra Campus, Jerusalem 91904, Israel

Ⓢ *Supporting Information*

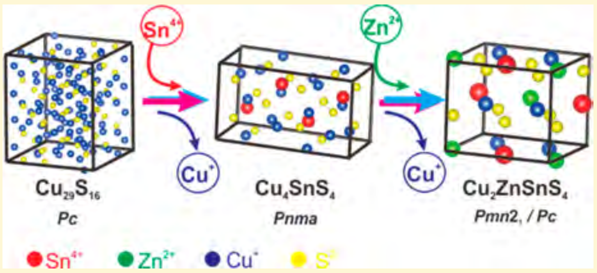

ABSTRACT: To control the process of cation exchange (CE) in a multielemental system, a detailed understanding of structural changes at the microscopic level is imperative. However, the synthesis of a multielemental system has so far relied on the CE phenomenon of a binary system, which does not necessarily extend to the higher-order systems. Here, direct experimental evidence supported by theoretical calculations reveals a growth model of binary Cu−S to ternary Cu−Sn−S to quaternary Cu−Zn−Sn−S, which shows that cations preferentially diffuse along a specific lattice plane with the preservation of sulfuric anionic framework. In addition, we also discover that, unlike the commonly accepted structure ($P6_3mc$), the metastable crystal structure of Cu−Zn−Sn−S phase possesses fixed Sn occupancy sites. By revealing the preferential nature of cations diffusion and growth mechanism, our work provides insight into controlling the stoichiometry and phase purity of novel multielemental materials.

INTRODUCTION

Chalcogenides are an important class of materials consisting of cations (M) and anions (sulfides, selenides, and tellurides) in the form of binary and multielemental (ternary and above) compounds.[1] As these materials exhibit valuable functional properties, they are widely used as light-absorbing materials, ionic conductors, catalysts, or phase-change materials and therefore are utilized in a broad range of applications, which include photovoltaic (PV), electronics, optics, and energy-storage materials.[2−13] The successful fabrication of functional devices often depends on the careful control of the material stoichiometry and phase purity. Unfortunately, when many elements are present, complex growth mechanisms and competing reaction kinetics hinder the formation of the desired phase.[8,14]

Advances in postsynthetic modification chemistry, specifically cation exchange (CE), provide pathways to previously unavailable nanomaterials including multielemental nanomaterials (e.g., metallo-organic framework, sulfides, oxides, and halides), epitaxial-core−shell, and epitaxial-hetero nanostructures.[15−22] Essentially, cation exchange enables tailoring of optical, electronic, and magnetic properties through transport of dissolved cations into the extended solid.[18,23−29] Two factors are necessary for successful CE: first, the Gibbs free energy of the products has to be lower than that of the reactants, and second, the CE reaction on the solid surface and in the extended solid must be kinetically favorable. However, despite the strong interest in multielemental materials, especially for solar cells, more CE work has been done on binary systems rather than ternary and quaternary systems. In particular, key problems to answer include nonuniform growth rates, preferential growth pathways, and competitive growth kinetics.[26,30,31] An ab initio calculation remains qualitative at best, and the control of materials formation requires a detailed understanding of events occurring during synthesis.[22,32,33] Further development in fundamental knowledge regarding nanomaterial formation via CE will enable further engineering of phase-pure multielemental materials for high-performance applications.

Here, a CE growth model that accounts for the temporal changes in crystal structures, the impact on the interfacial plane alignment of the heterophase, and the elemental distribution of

Received: July 19, 2017
Revised: October 1, 2017
Published: October 3, 2017

DOI: 10.1021/acs.chemmater.7b03029
Chem. Mater. 2017, 29, 9192−9199

the binary host component $Cu^{+}_{52}Cu^{2+}_{6}S_{32}^{2-}$ ($Cu_{58}S_{32}$) nanoparticles that form ternary $Cu^{+}_{4}Sn^{4+}S_{4}^{2-}$ (CTS) and quaternary $Cu^{+}_{2}Zn^{2+}Sn^{4+}S_{4}^{2-}$ (CZTS) systems will be presented sequentially. Currently, CZTS is a quaternary material explored for thin-film photovoltaic (PV) application due to its high solar absorption coefficient and makeup of abundant elements.[14,34−37] We show direct evidence of phase transformation from binary Cu−S to ternary Cu−Sn−S and quaternary Cu−Zn−Sn−S nanoparticles via ex situ temporal studies. High-resolution transmission electron microscopy (HRTEM) images shows preferential cations diffusion in the extended solid to proceed along a specific lattice plane due to the rigid sulfur anionic framework arrangement in the crystal matrix. Furthermore, we observed two types of alloyed CE reaction mechanism; the first is a positive cooperative mechanism for the growth of binary Cu−S to ternary Cu−Sn−S phase, and the second is a classical memoryless diffusion mechanism for the growth of ternary Cu−Sn−S phase to quaternary Cu−Zn−Sn−S phase. Lastly, with Z-contrast atomic-resolution TEM, the metastable crystal structure of quaternary Cu−Zn−Sn−S phase is revealed to possess fixed Sn occupancy sites, indicating that the crystal structure is $Pmn2_1$ or Pc, unlike the commonly accepted $P6_3mc$.[38] Our results demonstrate the complexity of multielemental material formation that involves multiple reaction processes in a single-phase transformation. This work highlights the imperativeness of understanding the reaction kinetics and elemental distribution at nanoscale during phase formation. In addition, by using a metastable crystal structure as a growth template, it provides insight for the synthesis of novel multielemental materials.

■ CATION-EXCHANGE PHENOMENON IN BINARY-TO-TERNARY CU CHALCOGENIDE

The main objective of this section is to understand the cation-exchange phenomenon in binary-to-ternary phase transformation (Cu−S to Cu−Sn−S) (Figure 1a). First, binary $Cu_{58}S_{32}$ nanoparticles are synthesized via heating-up method where copper(II) acetate is allowed to react with dodecanethiol at 230 °C for 60 min (refer to Methods for more detailed procedure). The binary-to-ternary transformation of Cu−S (Figures 1−3 in the Supporting Information) to Cu−Sn−S (Figures 4−6 in the Supporting Information) is proposed to occur via the following reactions, based on the X-ray diffraction (XRD) results (Figure 1vii−viii),

$$\frac{15}{2}Cu_{58}S_{32} + 8Sn^{4+} + 32e^{-} \rightarrow 8Cu_4SnS_4 + \frac{13}{2}Cu_{62}S_{32} \tag{1}$$

$$16Cu_{62}S_{32} + 8Sn^{4+} + 32e^{-} \rightarrow 8Cu_4SnS_4 + 15Cu_{64}S_{32} \tag{2}$$

$$Cu_{64}S_{32} + 8Sn^{4+} + 32e^{-} + \frac{32}{x}S \rightarrow 8Cu_4SnS_4 + \frac{32}{x}Cu_xS \tag{3}$$

where reactions 1, 2, and 3 are represented by the diffractograms collected at 0, 6, and 20 min, respectively (Figure 1viii), and energy-dispersive X-ray spectroscopy (EDX) shows increasing Sn incorporation as the reaction proceeds (Figure 7 in the Supporting Information). Surface-enhanced Raman spectroscopy (SERS) (Figure 1ix) confirms the incorporation of Sn into Cu−S as shown by the shift of the Cu−S vibration from 295 to 323 cm^{-1} as the reaction time increases.

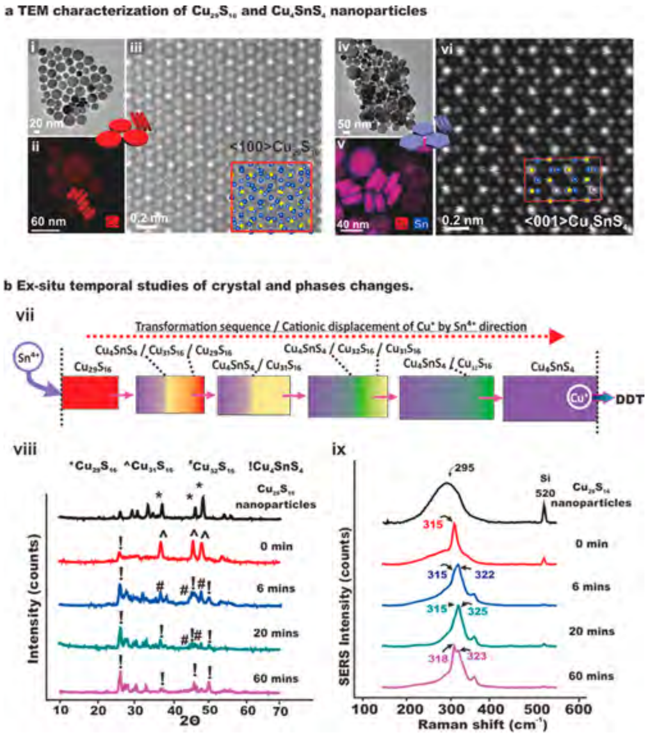

Figure 1. Ex situ temporal studies of $Cu_{29}S_{16}$ growth to Cu_4SnS_4. (a) TEM characterization of binary $Cu_{29}S_{16}$ nanoparticles and ternary Cu_4SnS_4 nanoparticles. Low magnification TEM (i, iv), scanning transmission electron microscopy-EDX (STEM-EDX) (ii, v), and HR-STEM (iii, vi) of $Cu_{29}S_{16}$ and Cu_4SnS_4 nanoparticles, respectively. (b) Pictorial illustration (vii) of ex situ temporal studies of crystal and phases changes characterized using XRD (viii) and SERS (ix).

First, in the CE of binary $Cu_{2-x}S$ nanoparticles, it was generally accepted that the free energies of formation for different $Cu_{2-x}S$ phases are in favor of higher stoichiometry ($Cu_{64}S_{32}$ is more preferred than $Cu_{62}S_{32}$).[39] However, our experiment does not agree with this suggestion as we found that a higher temperature is required to form $Cu_{64}S_{32}$ (~200 °C) as compared to $Cu_{62}S_{32}$ (~180 °C) (Figures 8−11 in the Supporting Information). Such a discrepancy may arise because cation exchange is a localized solid-state reaction whereas the previous report by Potter used electrochemical cells.[39] In addition, our experimental data is in good agreement with our density functional theory (DFT) calculation, which indicates that $Cu_{62}S_{32}$ is more favored because the calculated minimum $\Delta\mu_{Sn,eq1}$ is the smallest among the 3 eqs (Table 1 and Supporting Information Table 2; refer to Methods for more detailed procedures).

Following this, Jain and co-workers reported a rare CE exchange mechanism behaving similarly to the positive cooperatively binding of O_2 in blood hemoglobin.[31] In a positive cooperative CE reaction, successful cation displacement in nanoparticles increases the affinity for subsequent cation exchange. This encourages subsequent displacement to be in close proximity to the previous displaced site or an increase in the rate of successive displacement. To capture the CE of Sn into $Cu_{58}S_{32}$, we intentionally reduced the amount of Sn (Sn-poor condition). The elemental mapping by EDX indicates the positive cooperative CE reaction during the phase

Table 1. Calculated Chemical Potential Energy[a] of Sn and Zn

reaction equation	$Cu_{29}S_{16}$ + Sn (2)	$Cu_{31}S_{16}$ + Sn (3)	Cu_2S + Sn (4)	Cu_4SnS_4 + Zn (8)	theoretical mimimum chemical potential at equilibrium
$\Delta\mu_{Sn}$ (eV)	>−2.434	>2.422	>−0.778		−2.242
$\Delta\mu_{Zn}$ (eV)				>−1.797	−3.673

[a] $\Delta H_{eq2} = \sum \Delta H_{product} - \sum \Delta H_{reactant}$.

transformation of $Cu_{58}S_{32}$ to Cu_4SnS_4 (Figure 2a) with the phases identified by XRD (Figure 2ai and aii). We observe that Sn prefers to diffuse into heterostructure Cu−S/Cu−Sn−S nanoparticles (NPs) to form two different nanoparticles species (Cu_4SnS_4 and $Cu_{64}S_{32}$) as final product (Figure 12 in Supporting Information). When the amount of Sn-to-Cu ratio increases from (Cu/Sn 8:1 to 4:1), the percentage of Cu_4SnS_4 phase increases (Figure 2ai and aii), and elemental mapping by EDX still shows two different nanoparticles species (Cu_4SnS_4 and $Cu_{64}S_{32}$) as the final product. In both Cu/Sn ratio, we did not observe heterostructure Cu−S/Cu−Sn−S NPs as the final product. The incomplete reaction under Sn-poor condition can be explained by

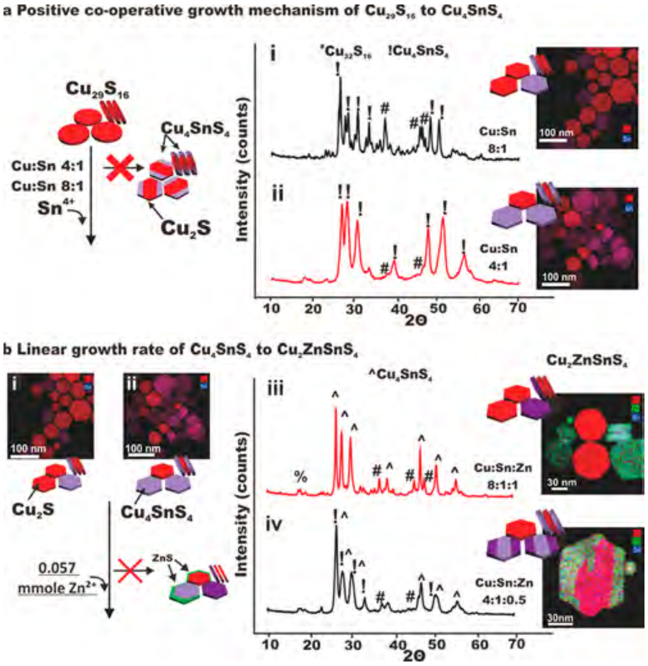

Figure 2. Linear and nonlinear growth rate. (a) XRD and STEM-EDX imaging of nanoparticles synthesized of Cu_4SnS_4 from $Cu_{29}S_{16}$ with Cu/Sn ratio 8:1 (i) and 4:1 (ii) showing positive cooperative growth phenomena. (b) XRD and STEM-EDX imaging of nanoparticles synthesized of Cu_2ZnSnS_4 with 0.057 mmol of Zn^{2+} with nanoparticles from 8:1 (i) and 4:1 (ii).

$$\Delta\mu_{Sn} = RT \ln \Delta c_{Sn} \tag{4}$$

where R is ideal gas constant, T is temperature, and Δc_{Sn} is the change in concentration of Sn^{4+} in the solution during reaction. From eq 4, when the concentration of Sn^{4+} decreases, the value of μ_{Sn} decreases as well; hence, the reaction will stop once μ_{Sn} decreases below the minimum chemical potential, therefore hindering complete reaction. The continuous depletion of Sn in the solution may also explain why DFT calculations cannot accurately predict the actual $\Delta\mu_{Sn}$ as a function of time. To conclude, we proposed that the binary ($Cu_{58}S_{32}$) to ternary (Cu_4SnS_4) transformation occurs through positive cooperative CE reaction.

CATION-EXCHANGE PHENOMENON IN TERNARY-TO-QUATERNARY CU CHALCOGENIDE

Next, from the XRD analysis, the cation-exchange reaction of Cu_4SnS_4 to Cu_2ZnSnS_4 can be expressed as (Figures 13−15 in Supporting Information) follows,

$$Cu_4SnS_4 + Zn^{2+} + S^{2-} \rightarrow Cu_2ZnSnS_4 + \frac{1}{32}Cu_{64}S_{32} \tag{5}$$

where Zn displaces Cu to form CZTS and $Cu_{64}S_{32}$ phases.

Two reactions under Zn-poor and equal Zn/Sn are carried out to understand how this cation-exchange reaction proceeds. Under Zn-poor conditions, uniformly distributed Cu−S, Cu−Sn−S, and heterostructured Cu_3SnS_4/Cu_2ZnSnS_4 nanoparticles can be observed (Figure 2b (iii, iv)). When equal Zn/Sn ratio is used, two different nanoparticle species ($Cu_{64}S_{32}$ and Cu_2ZnSnS_4) are observed (Figures 16 and 17 in the Supporting Information). This observation shows that the CE reaction of Cu_4SnS_4 to Cu_2ZnSnS_4 follows the classical memoryless, diffusion-limited CE process (i.e., as long as the cation can diffuse to a lattice site, exchange can take place at that site).[31] It is noted that, in both cases, there is no observable Zn−S rich phase from the elemental mapping. This can be easily understood for the Zn-poor case because there is insufficient Zn to form ZnS. However, when the ratio of Zn/Sn is ∼1, there is a possibility of forming ZnS phase. This prompted the need to investigate the reaction kinetics of Cu−Sn−S phase to CZTS phase formation under stoichiometric condition.

As the reaction coefficient (k_n) in the rate equation ($r_n = k_a[A]^x k_b[B]^y$) is affected by the activation energy (E_a) in the Arrhenius equation; $k_n = A\,e^{-E_a/RT}$,[40,41] the temperature at which the reaction occurs depends on the activation energy. Using ex situ XRD study, it is verified that the formation of Cu−S/Zn−S phase occurs at ∼200 °C, which is kinetically faster than the transformation of Cu−S to Cu−Sn−S (∼230 °C), while the Cu−Sn−S to CZTS transformation is kinetically the fastest reaction process (∼160 °C) (Figure 3 and Figures 18 and 19 in the Supporting Information). Hence, the relative reaction rates are ranked as r_3, Cu−Zn−Sn−S (160 °C) > r_4, Zn−S (200 °C) > r_1, Cu−S (230 °C) ≈ r_2, Cu−Sn−S (230 °C). Therefore, the absence of ZnS can be explained because of the preferential formation of Cu−Zn−Sn−S.

To conclude, we showed that the ternary (Cu_4SnS_4) to quaternary (Cu_2ZnSnS_4) transformation occurs through classical CE mechanism (Figure 20 in the Supporting Information). In addition, we also propose that a pure-phase Cu_2ZnSnS_4 can be obtained if the reaction is carried out at a temperature lower than the formation of the other secondary phases. After revealing the thermodynamic growth processes of Cu−S to Cu−Sn−S and to Cu−Zn−Sn−S, we perform further HRTEM analysis to identify the preferential diffusion pathways of the cations during the CE reaction.

SULFURIC ANIONIC FRAMEWORK DIRECTED CATION EXCHANGE

Alivisatos and co-workers showed that the anionic framework is preserved during CE for the binary system, while Lesnyak and

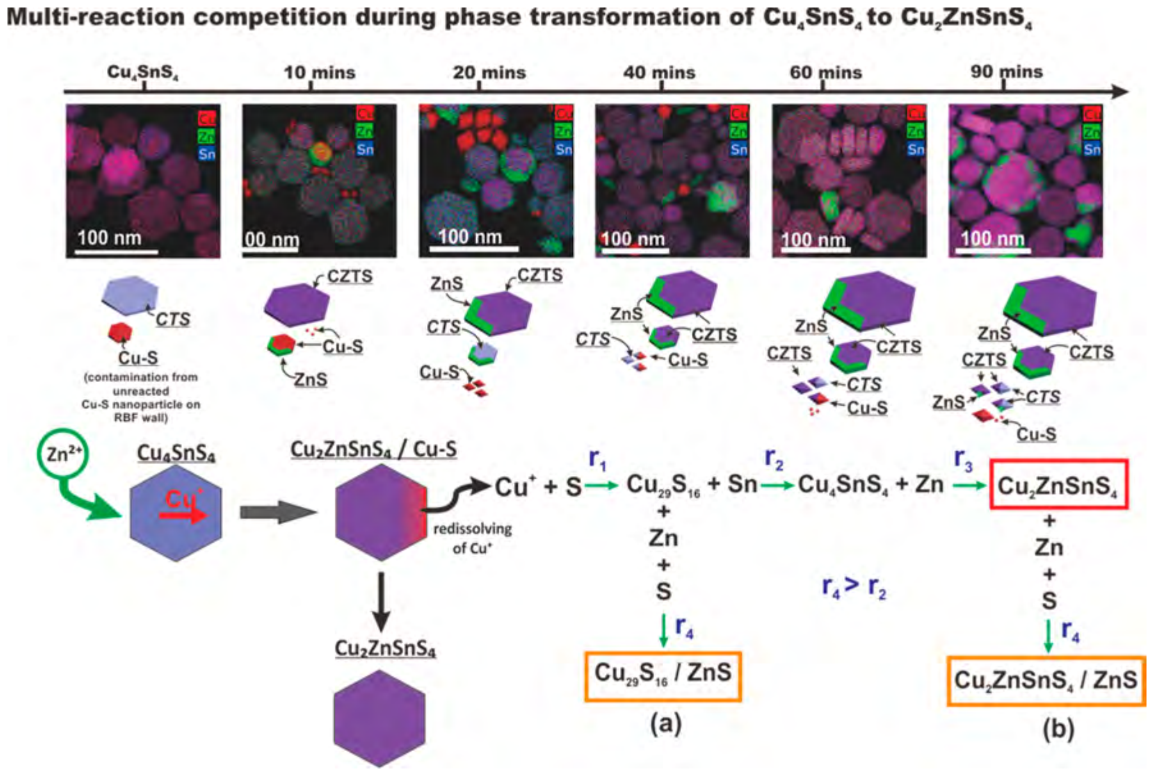

Figure 3. Conflicting reaction kinetics involved in a single-phase transformation process. (a) EDX mapping and schematic representation of multireaction competition occurring during conversion of Cu_4SnS_4 to Cu_2ZnSnS_4. The reaction kinetics of $Cu_{29}S_{16}$ to Cu_4SnS_4 conversion is shown to be limiting step due to higher reaction temperature as compared to conversion of Cu_4SnS_4 to Cu_2ZnSnS_4. The "wastage" of Zn^{2+} as a reaction kinetics r_4 is faster than r_2; therefore, in the long run the shortage of free Zn^{2+} prevents complete conversion of CTS to CZTS. As a result, multiphase nanomaterial is obtained at the end of reaction. See the Supporting Information for details. Cu−S, copper−sulfide derivatives; EDX, energy-dispersive X-ray spectroscopy.

co-workers showed the same for the binary to ternary and quaternary systems.[12,42] However, growth mechanisms are not reported in greater detail. In our study, direct imaging and characterization of $Cu_{58}S_{32}$ to Cu_4SnS_4 and Cu_2ZnSnS_4 phase growth using TEM revealed a preferential lattice transformation growth mechanism. By quenching the growth of $Cu_{58}S_{32}$ to Cu_4SnS_4 after 2 min of reaction, it freezes the transformation to reveal the lattice planes through which Sn^{4+} diffuses into $Cu_{58}S_{32}$. First, a homogeneous contrast at the interface of heterostructure Cu−S/Cu−Sn−S NPs using C_{3v} symmetry diffraction pattern masked on the HR-BFTEM (BFTEM = bright-field transmission electron microscopy) fast Fourier transform (FFT) image (Figure 4a and Supporting Information Figure 21) confirms the growth of $Cu_{58}S_{32}$ to Cu_4SnS_4 to follow the sulfuric anionic framework. Second, it is noted that the preferential diffusion of Sn^{4+} atoms is along the [012] plane of $Cu_{58}S_{32}$. The preferential diffusion along a longer pathway (across the NPs) instead of a shorter pathway (along the short axis) can be explained by the conservation of anionic framework and nanoplates morphology during the growth. Sulfur always arranges in hexagonal C_{3v} symmetry at the center of the S−M_4 (M = Sn, Cu) tetrahedral (Figure S22 in the Supporting Information). It is therefore kinetically less favorable for Sn to displace Cu with an S atom in the path.

Following, TEM imaging revealed the growth of Cu−Sn−S to Cu−Zn−Sn−S phase to follow a preferential lattice transformation growth mechanism (Figure 4b and Supporting Information Figure 23). First, as CTS phase and CZTS phase have similar FFT patterns (Figures 4, 13, and 20 in the Supporting Information), we are not able to differentiate the two phases from FFT. Therefore, by referring to the EDX data and HR-HAADF (HAADF = high-angle annular dark-field) imaging, the interfacial plane alignment between hetero CTS/CZTS involved the [010] plane of Cu_4SnS_4 and the [100] plane of Cu_2ZnSnS_4 (Figure 4vii) as Zn^{2+} diffuses along the [010] plane of Cu_4SnS_4 to form Cu_2ZnSnS_4 phase. In addition, during the growth of CZTS phase via CE, displacement of Cu by Zn resulted in the formation of hetero Cu−S/Cu−Zn−Sn−S particles intermediate. Using C_{3v} symmetry diffraction pattern masked on the HR-BFTEM FFT image (Figures 24 and 25 in the Supporting Information) shows a homogeneous contrast at the interface of hetero-(Cu−S/Cu−Zn−Sn−S), indicating the growth of Cu_4SnS_4 to Cu_2ZnSnS_4 to involve epitaxial displacement of Cu.

■ FIXED SN POSITION IN CU_2ZNSNS_4 METASTABLE CRYSTAL STRUCTURE

The generally accepted metastable structure of CZTS has $P6_3mc$ symmetry. This crystal structure can be summarized as (1) the structure is assumed to follow $P6_3mc$ wurtzite ZnS crystal structure and (2) cations (Cu, Zn, and Sn) randomly occupy the cation site of $P6_3mc$ ZnS crystal structure (Figure 26 in the Supporting Information). However, HR-STEM characterization of the CZTS nanoparticles indicates a fixed Sn occupancy (Figure 5a). By viewing the nanoparticles along three zone axes, two possible structures are identified to fit all three HR-HAADF zone-axis images. When Zn and Cu are assumed to follow Wurtzite-Stannite (WZ-S) arrangement, an

DOI: 10.1021/acs.chemmater.7b03029
Chem. Mater. 2017, 29, 9192−9199

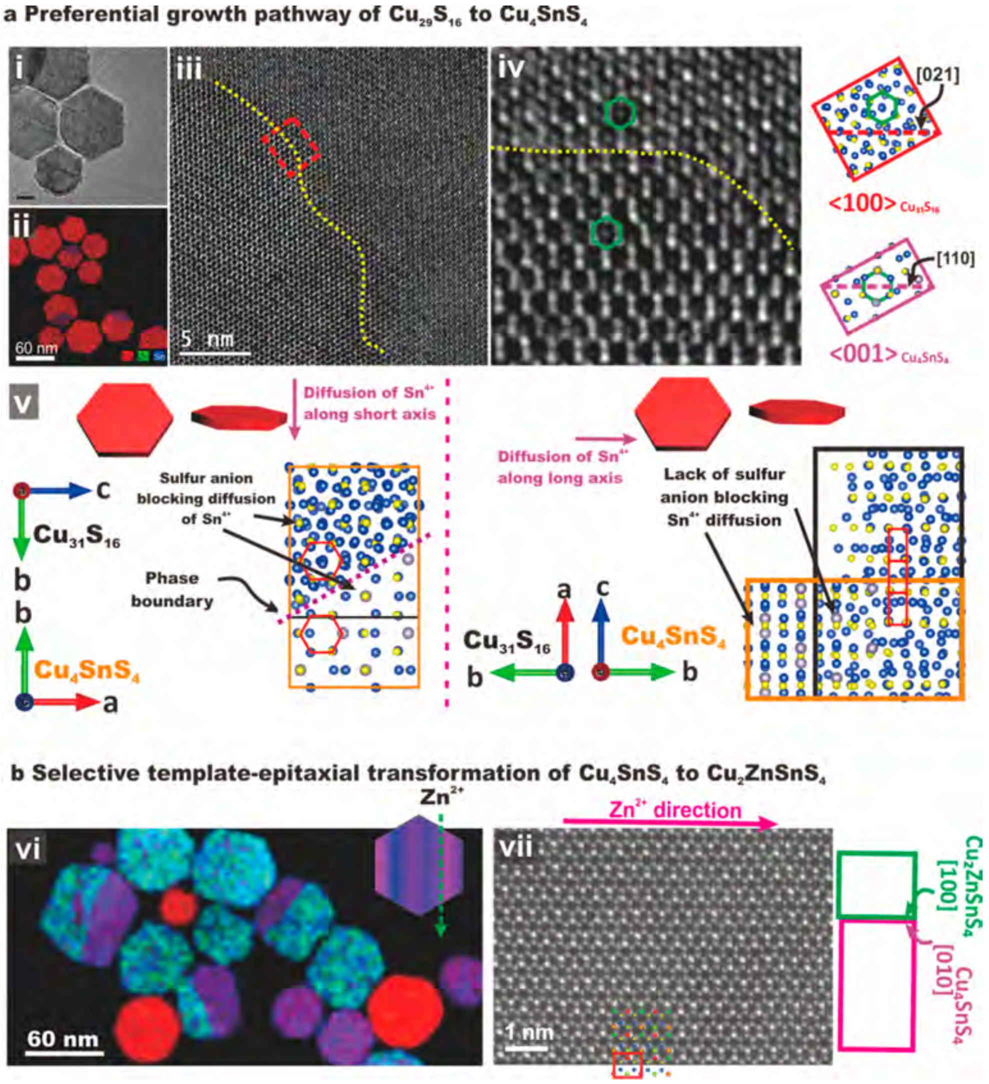

Figure 4. Preferential growth pathway of $Cu_{29}S_{16}$ to Cu_4SnS_4 to Cu_2ZnSnS_4 phase. (a) TEM imaging (i) and STEM-EDX mapping (ii) of heteronanoparticles ($Cu_{31}S_{16}$/Cu_4SnS_4), HR-TEM (iii, iv) showing the growth direction along the phase boundary, and pictorial illustration of sulfur anionic template influencing Sn^{4+} diffusion pathway (v). (b) Growth study of Cu_2ZnSnS_4 (Cu/Sn/Zn 4:1:0.5) quenched at 230 °C at 90 min with elemental mapping (vi), high-resolution TEM image and schematic illustration of growth direction showing phase separation during growth of Cu_4SnS_4 to Cu_2ZnSnS_4 (vii).

orthorhombic ($Pmn2_1$) crystal phase is obtained; whereas when Zn and Cu are assumed to follow Wurtzite-Kesterite (WZ-KS) arrangement, a monoclinic Pc crystal phase is obtained (Figure 5b and Figures 27 and 28 in the Supporting Information). Theoretical simulation of both WZ-KS and WZ-S shows nondistinguishable XRD patterns while DFT calculation showed a difference of only 0.011 eV between Pc CZTS (−3.673 eV) and $Pmn2_1$ CZTS (−3.663 eV). Therefore, this is indicative of equal possibility of either crystal structure or both being present (Table 3 in Supporting Information).

■ CONCLUSION

This work presents a model study to highlight the complexity of phase transition via cation exchange to form multicomponent sulfide nanomaterials ($Cu_{58}S_{32}$ to Cu_4SnS_4 to Cu_2ZnSnS_4). Ex situ temporal growth studies revealed that the phase transformation of binary $Cu_{58}S_{32}$ to ternary Cu_4SnS_4 to quaternary Cu_2ZnSnS_4 occurs via alloyed cation exchange in a fixed anionic framework. Tracing the structural changes of binary $Cu_{58}S_{32}$ growth to ternary Cu_4SnS_4 revealed a sequential three-step reaction involving two intermediate phases ($P2_1/n$ $Cu_{62}S_{32}$ and $P2_1/c$ $Cu_{64}S_{32}$) while preserving the anionic framework of $Cu_{58}S_{32}$. In our ex situ studies, we observed two types of alloyed CE reaction mechanism; the first is a positive cooperative mechanism for the growth of binary Cu−S to ternary Cu−Sn−S phase, and the second is a classical memoryless diffusion mechanism for the growth of ternary Cu−Sn−S phase to quaternary Cu−Sn−Sn−S phase.

Furthermore, the use of HR-HAADF imaging with Z-contrast capability enables the visualization of Sn fixed occupancy sites in our as-synthesized quaternary CZTS nanoparticles. This confirms that the crystal does not follow the commonly accepted $P6_3mc$ symmetry. However, due to the inability to distinguish Zn from Cu under Z-contrast, two crystal structures (WZ-KS and WZ-S) have been proposed with a small difference in energy (0.011 eV), hinting at an equal possibility in structural formation. This observation posed a potential challenge in future characterization of multicomponent material with conflicting crystal structures but similar X-ray diffraction patterns. The importance of accurate character-

DOI: 10.1021/acs.chemmater.7b03029
Chem. Mater. 2017, 29, 9192−9199

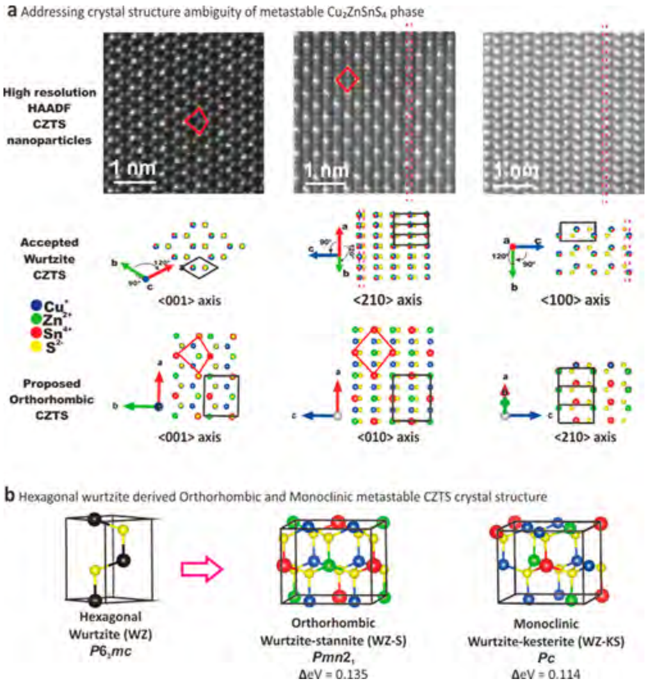

Figure 5. Determination of crystal structure via verification of 3-zone axis HR-HAADF image. (a) Verification of metastable CZTS crystal structure was carried out by taking HR-HAADF images of 3-zone axis. Due to the difference in Z-number contrast, Sn atom will appear the brightest. (b) Due to the inability to differentiate Cu to Zn, 2 crystal structures of orthorhombic WZ-S *Pmn*2$_1$ and monoclinic WZ-KS Pc are proposed to be the crystal structure of metastable CZTS.

ization of crystal structures and understanding the complex chemistry behind the growth of multicomponent materials will aid in future theoretical calculation, material designs and control of phase formation during the engineering of complex materials.

By understanding the growth dynamics, we can effectively pinpoint conflicting growth kinetics, allowing the planning of plausible solutions. This allows phase-pure nanoparticles to be synthesized. The advantage of a phase-pure nanoparticle (nanoink) approach includes bypassing random phase formation during thin-film fabrication as the phase (e.g., CZTS) is "preformed" during nanoparticles synthesis. As a result, it is desirable to develop a robust solution-based process for nanoparticles for the fabrication of nanoink-based devices.

■ METHODS

Synthesis of $Cu_{58}S_{32}$ Nanoparticles. $Cu(OCH_3)_2 \cdot H_2O$ (0.455 mmol) (Sigma-Aldrich, ≥98%) was added to 0.5 mL of oleylamine (Oam, Acros Organics, 80–90%) and 9 mL of 1-octadecene (Sigma-Aldrich, 90%) in a three-neck round-bottom flask (RBF) and allowed to heat to 130 °C under vacuum before adding 0.5 mL of dodecanethiol (DDT, Sigma-Aldrich, ≥98%) followed by further heating to 150 °C for 10 min under vacuum. The solution was then rapidly heated (10 °C/min) to 230 °C and reacted for 60 min under N_2 environment. The reaction was stopped by removing the RBF from the heating mantle and allowing it to naturally cool to 160 °C before placing it in a water bath for rapid cooling to 100 °C (for synthesis of $Cu_{32}Sn_8S_{32}$ nanoparticles) or room temperature (for characterization). Nanoparticles for characterization were washed via addition of 20 mL of hexane to the reaction solution, centrifuged at 10 000 rpm for 3 min for 3 times, and allowed to dry in a self-built N_2 box.

Synthesis of Cu_4SnS_4 Nanoparticles. A solution of Sn^{4+} salt (0.225 mmol of $Sn(Oac)_4$ (Sigma-Aldrich) dissolved in 1 mL of DDT and 1 mL of Oam) was added to $Cu_{58}S_{32}$ nanoparticles solution when it cooled to 80 °C. The reaction mixture was then heated rapidly (10 °C/min) to 150 °C under vacuum, followed by heating (10 °C/min) to 230 °C, and allowed to react for 60 min under N_2 environment. The reaction was stopped by removing the RBF from the heating mantle and allowing it to cool naturally to 160 °C before placing it in a water bath for rapid cooling to 100 °C (for synthesis of $Cu_{16}Zn_8Sn_8S_{32}$ nanoparticles) or room temperature (for characterization). Nanoparticles for characterization were washed via the addition of 20 mL of hexane to the reaction solution, centrifuged 3 times at 10 000 rpm for 3 min, and allowed to dry in a self-built N_2 box.

Synthesis of Sn-Poor Cu_4SnS_4 Nanoparticles. A solution of Sn^{4+} salt (0.113 mmol (halved) and 0.056 mmol (quartered) of $Sn(Oac)_4$ (Sigma-Aldrich) dissolved in 1 mL of DDT and 1 mL of Oam) was added to $Cu_{58}S_{32}$ nanoparticles solution when it cooled to 80 °C. The reaction mixture was then heated rapidly (10 °C/min) to 150 °C under vacuum, followed by heating (10 °C/min) to 230 °C, and allowed to react for 60 min under N_2 environment. The reaction was stopped by removing the RBF from the heating mantle and allowing it to cool naturally to 160 °C before placing it in a water bath for rapid cooling to 100 °C (for synthesis of $Cu_{16}Zn_8Sn_8S_{32}$ nanoparticles) or room temperature (for characterization). Nanoparticles for characterization were washed via the addition of 20 mL of hexane to the reaction solution, centrifuged 3 times at 10 000 rpm for 3 min, and allowed to dry in a self-built N_2 box.

Synthesis of Cu_2ZnSnS_4 Nanoparticles. $Zn(acac)_2 \cdot xH_2O$ (0.225 mmol) (assuming 1 part H_2O, Sigma-Aldrich powder) was added to $Cu_{32}Sn_8S_{32}$ nanoparticles solution when it cooled to 80 °C. The reaction mixture was then heated rapidly (10 °C/min) to 150 °C under vacuum, followed by heating (10 °C/min) to 240 °C, and allowed to react for 90 min under N_2 environment. The reaction was stopped by removing the RBF from the heating mantle and allowing it to cool naturally to 160 °C before placing it in a water bath for rapid cooling to room temperature. Nanoparticles for characterization were washed via addition of 20 mL of hexane to the reaction solution, centrifuged at 10 000 rpm for 3 min for 3 times, and allowed to dry in a self-built N_2 box.

Synthesis of Zn-Poor Cu_2ZnSnS_4 Nanoparticles. $Zn(acac)_2 \cdot xH_2O$ (0.056 mmol) (assuming 1 part H_2O, Sigma-Aldrich powder) was added to Sn-poor (0.113 mmol Sn^{4+}) nanoparticles dispersion when it cooled to 80 °C. The reaction mixture was then heated rapidly (10 °C/min) to 150 °C under vacuum, followed by heating (10 °C/min) to 240 °C, and allowed to react for 90 min under N_2 environment. The reaction was stopped by removing the RBF from the heating mantle and allowing it to cool naturally to 160 °C before placing it in a water bath for rapid cooling to room temperature. Nanoparticles for characterization were washed via addition of 20 mL of hexane to the reaction solution, centrifuged at 10 000 rpm for 3 min for 3 times, and allowed to dry in a self-built N_2 box.

Synthesis of Zn/Sn Equal Cu_2ZnSnS_4 Nanoparticles. $Zn(acac)_2 \cdot xH_2O$ (0.056 mmol) (assuming 1 part H_2O, Sigma-Aldrich powder) was added to Sn-poor (0.056 mmol Sn^{4+}) nanoparticles dispersion when it cooled to 80 °C. The reaction mixture was then heated rapidly (10 °C/min) to 150 °C under vacuum, followed by heating (10 °C/min) to 240 °C, and allowed to react for 90 min under N_2 environment. The reaction was stopped by removing the RBF from the heating mantle and allowing it to cool naturally to 160 °C before placing it in a water bath for rapid cooling to room temperature. Nanoparticles for characterization were washed via addition of 20 mL of hexane to the reaction solution, centrifuged at 10 000 rpm for 3 min for 3 times, and allowed to dry in a self-built N_2 box.

X-ray Diffraction. XRD samples were prepared by drop-casting a concentrated amount of nanoparticles solution on a Si wafer (1.5 × 1.5 cm) to form a thick and dense film. Patterns were recorded using Bruker D8 diffractometers running on Cu Kα radiation source ($\lambda 1$ = 1.54056 Å and $\lambda 2$ = 1.54439 Å) with a LynxEye detector and operated at 40 kV and 40 mA. All scan range were from 10° to 70°, with scan speed at 0.01° s^{-1}. All powder patterns were refined using the Topas. Quantitative Rietveld refinement wais carried out using the fundamental parameters approach, using accepted structural models obtained from the ICSD database of the respective components with just instrumental parameters refined, i.e., background (5-term Chebyshev polynomial, zero error, and "crystallite size" to model the microstructure-controlled line broadening).

Surface-Enhanced Raman Scattering. A 50 nm thick Ag film on Si (10 nm Cr coating) was prepared using thermal evaporation to serve as substrate for SERS spectroscopy characterization of as-synthesized nanoparticles. Diluted nanoparticle solutions in hexane were then drop-casted (5 μL, 4 mg/mL) onto an Ag-coated Cr/Si wafer (5 mm × 5 mm) to form a thin film for SERS measurements. SERS spectra were obtained with the sample mounted on the Ramantouch microspectrometer (Nanophoton, Inc., Osaka, Japan). A 532 nm laser was used as the excitation laser. The excitation laser light was focused into a line (x−y axis line scan mode) on a sample through a cylindrical lens and an air objective lens (LU Plan Fluor 100× NA 0.9). The excitation laser power is 0.04 mW with exposure time for each line and slit width of the spectrometer being 30 s and 50 μm, respectively. The final SERS spectrum is an average of all the spectra collected (300 spectra).

TEM Analysis. TEM sample preparation involved dripping 1 drop of diluted nanoparticles solution (4 mg/mL) on a pure carbon Ni grid (Ted Pella) and allowing it to dry before dripwise washing it with 1 mL of toluene. High-resolution bright-field (HR-BF) transmission electron microscopy (TEM) was carried out on a TECNAI F20 operating at an accelerating voltage of 200 kV. High-resolution high annular angular dark field (HR-HAADF) scanning TEM image was carried out on TEAM 0.5 (a modified FEI Titan 80−300 microscope equipped with a high-brightness Schottky-field emission electron source with two CEOS hexapole-type spherical aberration correctors) operating at an acceleration voltage of 300 kV. X-ray dispersion energy spectrum (EDS) mapping was carried out on TitanX (FEI TitanX 60−300 microscope equipped with Bruker windowless EDS detector with a solid angle of 0.7 steradians enables high count rates with minimal dead time) operating at 200 kV at 80k× magnification, 0.68 nA beam current, 2068 × 2068 pixel resolution, with a dwell time of 15 min and an average signal count of >1000 per pixel. Fast Fourier transform (FFT) and inverse FFT are carried out using Gatan Microscope Suite and ES Vision.

Density Functional Theory Calculations. First-principle modeling to calculate the formation energies of each process using the Vienna ab initio simulation package (VASP) is employed. The projector augmented wave (PAW) method is used to describe the electron−ion interaction, and the exchange correlation between electrons is described by the generalized gradient approximation (GGA) in the Perdew−Burke−Ernzerhof (PBE) form. Although the PBE functional cannot correctly describe the band structures of CZTS, the energy differences between difference phases are precise enough. We used a cutoff energy of 350 eV for the plane-wave basis set. For different compounds, different k-mesh settings within the Monkhorst−Pack scheme are used. Lattice relaxation was continued until the forces on all the atoms were converged to $<10^{-2}$ eV Å^{-1}. The volume of the supercell was fixed, but all the internal freedoms were fully relaxed. The lattice constants reproduced from GGA-PBE computations, as well as the theoretical and experimental values from the literature, are listed in Table 1 in the Supporting Information. From the table, we found out that our calculated lattice parameters agree well with the experimental values. After relaxing the geometric structures, the formation enthalpy energies of different compounds can be calculated as

$$\Delta H_{\mathrm{f}} = E_{\mathrm{solid}} - n_\alpha \sum_\alpha E_\alpha{}^{\mathrm{bulk}}$$

where E_{solid} is the total energy of a given bulk compound, n_α is the number of α element in compound, and $E_\alpha{}^{\mathrm{bulk}}$ is the energy per atom of pure α in its standard elemental phase. In this study, the standard phase of the Cu, Zn, Sn, and S elements are FCC-Cu, FCC-Zn, alpha-Sn, and alpha-S (S_8), respectively. The calculated results are also listed in Table 1 in the Supporting Information.

■ ASSOCIATED CONTENT

Ⓢ Supporting Information

The Supporting Information is available free of charge on the ACS Publications website at DOI: 10.1021/acs.chemmater.7b03029.

> Additional TEM images, XRD, Rietveld refinements, crystal structure parameters, XPS, SERS spectra, and EDX measurements of as-synthesized CS, CTS, and CZTS nanoparticles (PDF)

■ AUTHOR INFORMATION

ORCID

Srikanth Pedireddy: 0000-0002-4315-390X
Xingyi Ling: 0000-0001-5495-6428
Shlomo Magdassi: 0000-0002-6794-0553
Shuzhou Li: 0000-0002-2159-2602
Haimei Zheng: 0000-0003-3813-4170
Lydia H. Wong: 0000-0001-9059-1745

Author Contributions

J.M.R.T. and L.H.W. conceived and designed this project. J.M.R.T. carried out material synthesis and material phase characterization using XRD and Raman spectroscopy. J.M.R.T., C.T.N., M.S., and R.T. carried out TEM experiments. S.P. carried out XPS characterization. W.H. carried out DFT calculation. J.M.R.T. and T.B. carried out Rietveld refinement. All authors discussed and analyzed the data. J.M.R.T., M.S., T.B., W.H., S.M., T.W., and L.H.W. wrote the manuscript.

Notes

The authors declare no competing financial interest.

■ ACKNOWLEDGMENTS

We acknowledge financial support from National Research Foundation (NRF), Singapore, through the Singapore-Berkeley Research Initiative for Sustainable Energy (SinBeRISE) and Nanomaterials for Energy and Water Management (SHARE NEW) CREATE program. L.H.W. thanks the funding support from Singapore Ministry of Education, Tier 2 (2016-T2-1-030). S.L. acknowledges the funding support from Singapore Ministry of Education Tier 1 (107/15). H.Z. thanks the funding support from U.S. DOE BES Materials Sciences and Engineering Division Under Contract No. KC22ZH. X.Y.L. thanks the funding support from Singapore Ministry of Education, Tier 1 (RG21/16) and Tier 2 (MOE2016-T2-1-043) grants.. The work at the Molecular Foundry was supported by the Office of Science, Office of Basic Energy Sciences, of the U.S. Department of Energy under Contract No. DE-AC02-05CH11231. We thank Fiona Doyle for lending us her synthetic laboratory in University of California Berkeley (UCB), Song Chengyu and Karen Bustilo for their help and assistance on TEM, and Matthew P. Sherburne for nanoparticle growth discussion.

■ REFERENCES

(1) Greenwood, N. N.; Earnshaw, A. *Chemistry of the Elements*; Elsevier: 2012.

(2) Eggleton, B. J.; Luther-Davies, B.; Richardson, K. Chalcogenide photonics. *Nat. Photonics* **2011**, *5*, 141−148.

(3) Wang, Q. H.; Kalantar-Zadeh, K.; Kis, A.; Coleman, J. N.; Strano, M. S. Electronics and optoelectronics of two-dimensional transition metal dichalcogenides. *Nat. Nanotechnol.* **2012**, *7*, 699−712.

(4) Armatas, G. S.; Kanatzidis, M. G. Mesoporous germanium-rich chalcogenido frameworks with highly polarizable surfaces and relevance to gas separation. *Nat. Mater.* **2009**, *8*, 217−222.

(5) Sivula, K.; van de Krol, R. Semiconducting materials for photoelectrochemical energy conversion. *Nat. Rev. Mater.* **2016**, *1*, 15010.

(6) Wuttig, M.; Yamada, N. Phase-change materials for rewriteable data storage. *Nat. Mater.* **2007**, *6*, 824−832.

(7) Gao, M.-R.; Xu, Y.-F.; Jiang, J.; Yu, S.-H. Nanostructured metal chalcogenides: synthesis, modification, and applications in energy conversion and storage devices. *Chem. Soc. Rev.* **2013**, *42*, 2986−3017.

(8) Polizzotti, A.; Repins, I. L.; Noufi, R.; Wei, S.-H.; Mitzi, D. B. The state and future prospects of kesterite photovoltaics. *Energy Environ. Sci.* **2013**, *6*, 3171−3182.

(9) Zheng, N.; Bu, X.; Feng, P. Synthetic design of crystalline inorganic chalcogenides exhibiting fast-ion conductivity. *Nature* **2003**, *426*, 428−432.

(10) Acerce, M.; Voiry, D.; Chhowalla, M. Metallic 1T phase MoS2 nanosheets as supercapacitor electrode materials. *Nat. Nanotechnol.* **2015**, *10*, 313−318.

(11) De Trizio, L.; Li, H.; Casu, A.; Genovese, A.; Sathya, A.; Messina, G. C.; Manna, L. Sn Cation Valency Dependence in Cation Exchange Reactions Involving Cu2-xSe Nanocrystals. *J. Am. Chem. Soc.* **2014**, *136*, 16277−16284.

(12) Akkerman, Q. A.; Genovese, A.; George, C.; Prato, M.; Moreels, I.; Casu, A.; Marras, S.; Curcio, A.; Scarpellini, A.; Pellegrino, T.; Manna, L.; Lesnyak, V. From Binary Cu2S to Ternary Cu−In−S and Quaternary Cu−In−Zn−S Nanocrystals with Tunable Composition via Partial Cation Exchange. *ACS Nano* **2015**, *9*, 521−531.

(13) Lesnyak, V.; George, C.; Genovese, A.; Prato, M.; Casu, A.; Ayyappan, S.; Scarpellini, A.; Manna, L. Alloyed Copper Chalcogenide Nanoplatelets via Partial Cation Exchange Reactions. *ACS Nano* **2014**, *8*, 8407−8418.

(14) Zhou, H.; Hsu, W.-C.; Duan, H.-S.; Bob, B.; Yang, W.; Song, T.-B.; Hsu, C.-J.; Yang, Y. CZTS nanocrystals: a promising approach for next generation thin film photovoltaics. *Energy Environ. Sci.* **2013**, *6*, 2822−2838.

(15) Krogstrup, P.; Ziino, N. L. B.; Chang, W.; Albrecht, S. M.; Madsen, M. H.; Johnson, E.; Nygård, J.; Marcus, C. M.; Jespersen, T. S. Epitaxy of semiconductor−superconductor nanowires. *Nat. Mater.* **2015**, *14*, 400−406.

(16) Tang, J.; Huo, Z.; Brittman, S.; Gao, H.; Yang, P. Solution-processed core-shell nanowires for efficient photovoltaic cells. *Nat. Nanotechnol.* **2011**, *6*, 568−572.

(17) Nouar, F.; Eckert, J.; Eubank, J. F.; Forster, P.; Eddaoudi, M. Zeolite-like Metal−Organic Frameworks (ZMOFs) as Hydrogen Storage Platform: Lithium and Magnesium Ion-Exchange and H2-(rho-ZMOF) Interaction Studies. *J. Am. Chem. Soc.* **2009**, *131*, 2864−2870.

(18) Nedelcu, G.; Protesescu, L.; Yakunin, S.; Bodnarchuk, M. I.; Grotevent, M. J.; Kovalenko, M. V. Fast Anion-Exchange in Highly Luminescent Nanocrystals of Cesium Lead Halide Perovskites (CsPbX3, X = Cl, Br, I). *Nano Lett.* **2015**, *15*, 5635−5640.

(19) Manthiram, A.; Kim, J. Low Temperature Synthesis of Insertion Oxides for Lithium Batteries. *Chem. Mater.* **1998**, *10*, 2895−2909.

(20) Wang, D.-Y.; Chen, C.-H.; Yen, H.-C.; Lin, Y.-L.; Huang, P.-Y.; Hwang, B.-J.; Chen, C.-C. Chemical Transformation from FePt to Fe1-xPtMx (M = Ru, Ni, Sn) Nanocrystals by a Cation Redox Reaction: X-ray Absorption Spectroscopic Studies. *J. Am. Chem. Soc.* **2007**, *129*, 1538−1540.

(21) Beberwyck, B. J.; Alivisatos, A. P. Ion Exchange Synthesis of III−V Nanocrystals. *J. Am. Chem. Soc.* **2012**, *134*, 19977−19980.

(22) Kwon, S. G.; Krylova, G.; Phillips, P. J.; Klie, R. F.; Chattopadhyay, S.; Shibata, T.; Bunel, E. E.; Liu, Y.; Prakapenka, V. B.; Lee, B.; Shevchenko, E. V. Heterogeneous nucleation and shape transformation of multicomponent metallic nanostructures. *Nat. Mater.* **2015**, *14*, 215−223.

(23) Yu, J. H.; Liu, X.; Kweon, K. E.; Joo, J.; Park, J.; Ko, K.-T.; Lee, D. W.; Shen, S.; Tivakornsasithorn, K.; Son, J. S.; Park, J.-H.; Kim, Y.-W.; Hwang, G. S.; Dobrowolska, M.; Furdyna, J. K.; Hyeon, T. Giant Zeeman splitting in nucleation-controlled doped CdSe:Mn2+ quantum nanoribbons. *Nat. Mater.* **2010**, *9*, 47−53.

(24) Beberwyck, B. J.; Surendranath, Y.; Alivisatos, A. P. Cation Exchange: A Versatile Tool for Nanomaterials Synthesis. *J. Phys. Chem. C* **2013**, *117*, 19759−19770.

(25) Gupta, S.; Kershaw, S. V.; Rogach, A. L. 25th Anniversary Article: Ion Exchange in Colloidal Nanocrystals. *Adv. Mater.* **2013**, *25*, 6923−6944.

(26) Aldakov, D.; Lefrancois, A.; Reiss, P. Ternary and quaternary metal chalcogenide nanocrystals: synthesis, properties and applications. *J. Mater. Chem. C* **2013**, *1*, 3756−3776.

(27) Caban-Acevedo, M.; Stone, M. L.; Schmidt, J. R.; Thomas, J. G.; Ding, Q.; Chang, H.-C.; Tsai, M.-L.; He, J.-H.; Jin, S. Efficient hydrogen evolution catalysis using ternary pyrite-type cobalt phosphosulphide. *Nat. Mater.* **2015**, *14*, 1245−1251.

(28) De Trizio, L.; Manna, L. Forging Colloidal Nanostructures via Cation Exchange Reactions. *Chem. Rev.* **2016**, *116*, 10852−10887.

(29) Rivest, J. B.; Jain, P. K. Cation exchange on the nanoscale: an emerging technique for new material synthesis, device fabrication, and chemical sensing. *Chem. Soc. Rev.* **2013**, *42*, 89−96.

(30) Anderson, B. D.; Tracy, J. B. Nanoparticle conversion chemistry: Kirkendall effect, galvanic exchange, and anion exchange. *Nanoscale* **2014**, *6*, 12195−12216.

(31) White, S. L.; Smith, J. G.; Behl, M.; Jain, P. K. Co-operativity in a nanocrystalline solid-state transition. *Nat. Commun.* **2013**, *4*, 3933.

(32) Jacobsson, D.; Panciera, F.; Tersoff, J.; Reuter, M. C.; Lehmann, S.; Hofmann, S.; Dick, K. A.; Ross, F. M. Interface dynamics and crystal phase switching in GaAs nanowires. *Nature* **2016**, *531*, 317−322.

(33) Tan, J. M. R.; Lee, Y. H.; Pedireddy, S.; Baikie, T.; Ling, X. Y.; Wong, L. H. Understanding the Synthetic Pathway of a Single-Phase Quarternary Semiconductor Using Surface-Enhanced Raman Scattering: A Case of Wurtzite Cu2ZnSnS4 Nanoparticles. *J. Am. Chem. Soc.* **2014**, *136*, 6684−6692.

(34) Mitzi, D. B.; Gunawan, O.; Todorov, T. K.; Wang, K.; Guha, S. The path towards a high-performance solution-processed kesterite solar cell. *Sol. Energy Mater. Sol. Cells* **2011**, *95*, 1421−1436.

(35) Su, Z.; Tan, J. M. R.; Li, X.; Zeng, X.; Batabyal, S. K.; Wong, L. H. Cation Substitution of Solution-Processed Cu2ZnSnS4 Thin Film Solar Cell with over 9% Efficiency. *Adv. Energy. Mater.* **2015**, *5*, 1500682.

(36) Singh, A.; Geaney, H.; Laffir, F.; Ryan, K. M. Colloidal Synthesis of Wurtzite Cu2ZnSnS4 Nanorods and Their Perpendicular Assembly. *J. Am. Chem. Soc.* **2012**, *134*, 2910−2913.

(37) Shavel, A.; Cadavid, D.; Ibáñez, M.; Carrete, A.; Cabot, A. Continuous Production of Cu2ZnSnS4 Nanocrystals in a Flow Reactor. *J. Am. Chem. Soc.* **2012**, *134*, 1438−1441.

(38) Mainz, R.; Singh, A.; Levcenko, S.; Klaus, M.; Genzel, C.; Ryan, K. M.; Unold, T. Phase-transition-driven growth of compound semiconductor crystals from ordered metastable nanorods. *Nat. Commun.* **2014**, *5*, 4133.

(39) Potter, R. W. An electrochemical investigation of the system copper-sulfur. *Econ. Geol. Bull. Soc. Econ. Geol.* **1977**, *72*, 1524−1542.

(40) McNaught, A. D.; McNaught, A. D. *Compendium of chemical terminology*; Blackwell Science: Oxford, U.K., 1997; Vol. *1669*.

(41) Laidler, K. J. The development of the Arrhenius equation. *J. Chem. Educ.* **1984**, *61*, 494−498.

(42) Jain, P. K.; Amirav, L.; Aloni, S.; Alivisatos, A. P. Nanoheterostructure Cation Exchange: Anionic Framework Conservation. *J. Am. Chem. Soc.* **2010**, *132*, 9997−9999.

DOI: 10.1021/acs.chemmater.7b03029